Check for updates

ADVANCED ENGINEERING MATERIALS
www.aem-journal.com

Profilometry-Based Indentation Plastometry at High Temperature

*Hannes Tammpere, Phil McKeown, James Miller, Chizhou Fang, Emily Curtis, Marcus Gaiser-Porter, Max Burley, James Campbell, Maria Artiles, Yuanbo Tang, Satesh Utada, Roger Reed, and Trevor Clyne**

This is a first report on profilometry-based indentation plastometry (PIP) at high temperature (HT), covering both thermal characterization and issues for obtaining stress–strain curves. The heating system has a relatively low thermal inertia, reaching 800 °C within about 10 min, while both indentation (≈20 s) and cooling (≈20 min) are also quick. This capability is useful in terms of limiting exposure of the sample to prolonged periods at HT, and hence avoiding the formation of thick oxide layers (which can affect indent profiles and hence inferred stress–strain curves). There is good general consistency between stress–strain curves obtained via HT-PIP and those from tensile testing. However, the possibility of creep (time-dependent deformation) affecting the outcomes (of both types of test), particularly at higher temperatures, should be borne in mind. Creep has a characteristic effect on tensile curves, which can often be confirmed and investigated by changing the imposed strain rate. It can also be revealed by carrying out the HT-PIP testing with different penetration velocities or by monitoring the shape of the load–displacement plot.

1. Introduction

The PIP (profilometry-based indentation plastometry) procedure is now a well-established mechanical testing technique. It has evolved from more than two decades of research aimed at procedures for inferring stress–strain relationships from outcomes of instrumented indentation tests. Much early work involved use of nanoindenters, with the instrumentation often relating primarily to the acquisition of load–displacement data and a progressive focus on reducing the scale of the indentation. The most popular methodology was based initially[1–7] on direct conversion (using empirical relationships) of the load to an equivalent stress and the displacement to an equivalent strain—this is sometimes referred to as the instrumented indentation technique. This approach is attractively simple, but it eventually became clear[8] that such conversions cannot capture the complexity of the evolving stress and strain fields during indentation and do not lead to reliable stress–strain relationships being obtainable in a universal way.

The procedure that has evolved into a commercially viable methodology is that of iterative finite element method (FEM) simulation of the indentation,[9–15] converging on the stress–strain relationship (captured in a constitutive law) that gives optimal agreement between measured and modeled outcomes. It has also been shown[16–19] that there are important advantages to using the indent profile, rather than the load–displacement curve, as the target outcome. This methodology is conceptually simple and rigorous, but the development of commercially viable stand-alone products has required optimization of control and simulation software, linked to equipment for automated creation and characterization of suitable indents. A further important advance has been the recognition that if scale-independent

H. Tammpere, P. McKeown, J. Miller, C. Fang, M. Gaiser-Porter, M. Burley, J. Campbell, M. Artiles, T. Clyne
Plastometrex Ltd
204 Science Park, Milton Road, Cambridge CB4 0GZ, UK
E-mail: twc10@cam.ac.uk

The ORCID identification number(s) for the author(s) of this article can be found under https://doi.org/10.1002/adem.202301073.

© 2024 The Author(s). Advanced Engineering Materials published by Wiley-VCH GmbH. This is an open access article under the terms of the Creative Commons Attribution License, which permits use, distribution and reproduction in any medium, provided the original work is properly cited.

DOI: 10.1002/adem.202301073

E. Curtis, T. Clyne
Department of Materials Science
University of Cambridge
27 Charles Babbage Road, Cambridge CB3 0FS, UK

Y. Tang, R. Reed
School of Metallurgy and Materials
University of Birmingham
Elms Road, Birmingham B15 2SE, UK

S. Utada
Research Centre for Structural Materials
NIMS
305-0047 1-2-1 Sengen, Tsukuba Ibaraki, Japan

R. Reed
Department of Materials
University of Oxford
Parks Road, Oxford OX1 3PH, UK

15272648, 0, Downloaded from https://onlinelibrary.wiley.com/doi/10.1002/adem.202301073 by National Institute For, Wiley Online Library on [23/09/2024]. See the Terms and Conditions (https://onlinelibrary.wiley.com/terms-and-conditions) on Wiley Online Library for rules of use; OA articles are governed by the applicable Creative Commons License

stress–strain relationships are being sought, then the volume being deformed must be large enough to be representative of the bulk, which usually translates into it containing a relatively large number of grains. In most cases, nanoindenters are not suitable for this. There are also certain other requirements, such as a need[13,20] to create plastic strains in the range of up to at least a few tens of %.

Recent work has covered application of the PIP technique to a wide range of materials and effects. These include study of welds,[21] pipelines,[22] additively manufactured components,[23,24] metal matrix composites,[25] effects of residual stress,[26] case-hardened layers,[27] very hard metals,[28] and porous metals.[29] There is also a review article[30] that covers various aspects of the methodology. Consultation of this article is recommended because many details of the way that the modeling is carried out are covered there. These include use of the Voce equation[31] as the constitutive law of choice. The advantages of PIP (particularly in comparison with tensile testing), which partly concern ease of sample preparation and speed of testing, are arguably even more significant for characterization of plasticity at high temperature (HT). There may be benefits in minimizing the period spent at HT, to reduce microstructural changes, and this is likely to be easier with the relatively small, flat samples used in PIP testing.

While the relatively small size of PIP samples allows use of a hot stage with low thermal inertia, the fact that the tested region is not very small—it is typically about 1 mm in lateral extent and 200 μm deep—ensures that the problems of thermal drift and instability that are commonly encountered when using nanoindenters at HT (or even at room temperature[32]) can be avoided. As for room temperature operation, the "intermediate" scale of PIP has the potential to allow speed and simplicity of testing in combination with a rigor comparable to that of tensile testing. Nevertheless, elevated temperature certainly introduces new technical challenges for PIP testing. This article describes the development of a commercial HT PIP (HT-PIP) setup and presents data related to its operation.

2. Materials and Test Procedures

2.1. Materials

The testing program involved a total of six materials (see **Table 1**), which gives the compositions and suppliers. The DS Cu was only used in thermal trials (representative of metals with high thermal conductivity), but the others were all subjected to mechanical testing (using both tensile and HT-PIP tests). They exhibit a wide range of thermomechanical characteristics.

2.2. HT Tensile Testing

Most of the tensile testing was carried out in Cambridge using an Instron 3369 loading frame, with a Severn Thermal Solutions Furnace. The tensile samples were cylindrical, with threaded ends. The reduced section length was 29 mm, with a diameter of 5 mm, and the clip gauge length was 25 mm. The ceramic knife-edges of the clip gauge come through a small slot in the furnace wall, while three thermocouples (to be touching the sample within the gauge length) are introduced from the other side of the furnace. Samples were heated at 10 K min^{-1} for the SS310 and S690QL samples and 20 K min^{-1} for the C-300. In both cases, there was a 20 min soak prior to the start of the test. The standard displacement rate during loading was 10 mm min^{-1}, corresponding to a strain rate of about 7×10^{-3} s^{-1}.

For testing of the Waspaloy and Al-2618, undertaken at Oxford, an Instron 8862 loading frame was used, with the same type of furnace. These samples were also cylindrical, with a gauge diameter of 3.5 mm and a gauge length of 6 mm. Straining was monitored via an Imetrum video extensometry system, with viewing through a quartz window in the furnace wall. Heating was at 25 K min^{-1} with a 10 min soak prior to the start of the test. The displacement rate during loading was 3.6 mm min^{-1}, corresponding to a strain rate of about 10^{-2} s^{-1}. The standard strain rates used in the two laboratories were therefore very similar.

2.3. HT-PIP Testing

2.3.1. Hot Stage

The hot stage, for integration into a standard benchtop plastometer, is depicted schematically in **Figure 1**. The glass–ceramic disks have a very low thermal conductivity ($K \approx 1$ W m^{-1} K^{-1}). The air ($K \approx 0.025$ W m^{-1} K^{-1}) gap also presents a large thermal barrier, with the air jet ensuring that there is no recirculatory convective heat flow between the load cell platen and the location plate. The silicon nitride (ball) is not a good thermal conductor

Table 1. Codes, nominal compositions, and suppliers of the metals used. SS310 is a (high-Cr) austenitic stainless steel, S690QL is a "high-speed steel" (HSS), Al-2618 is an age-hardening Al alloy, Waspaloy is a Ni-based superalloy, C-300 is a maraging steel, and DS Cu is dispersion strengthened copper (containing alumina particles).

Code	Composition [wt%]														Supplier
	C	Si	Mn	Co	Mo	Cr	Ni	S	P	Cu	Fe	Mg	Al	Ti	
SS310	0.25	1.5	2.0	–	–	25	20	0.03	0.04	0.5	bal.	–	–	–	Neonickel
S690QL	0.20	0.8	1.7	–	0.7	1.5	2.0	0.001	0.012	0.5	bal.	–	–	–	Brown-MacFarlane
Al-2618	–	0.2	0.02	–	–	–	1.1	–	–	2.4	1.1	1.5	bal.	0.05	Dynamic Metals
Waspaloy	0.04	0.03	0.03	12.3	3.8	19.3	bal.	0.001	0.003	0.02	1.5	–	1.3	3.0	Neonickel
C-300	0.01	0.04	0.02	9.3	4.8	0.13	18.2	0.001	0.005	0.07	bal.	–	0.1	0.7	Dynamic Metals
DS Cu	–	–	–	–	–	–	–	–	–	bal.	–	–	7.0 Al_2O_3	–	Gadi Co. Inc.

 © 2024 The Author(s). Advanced Engineering Materials published by Wiley-VCH GmbH

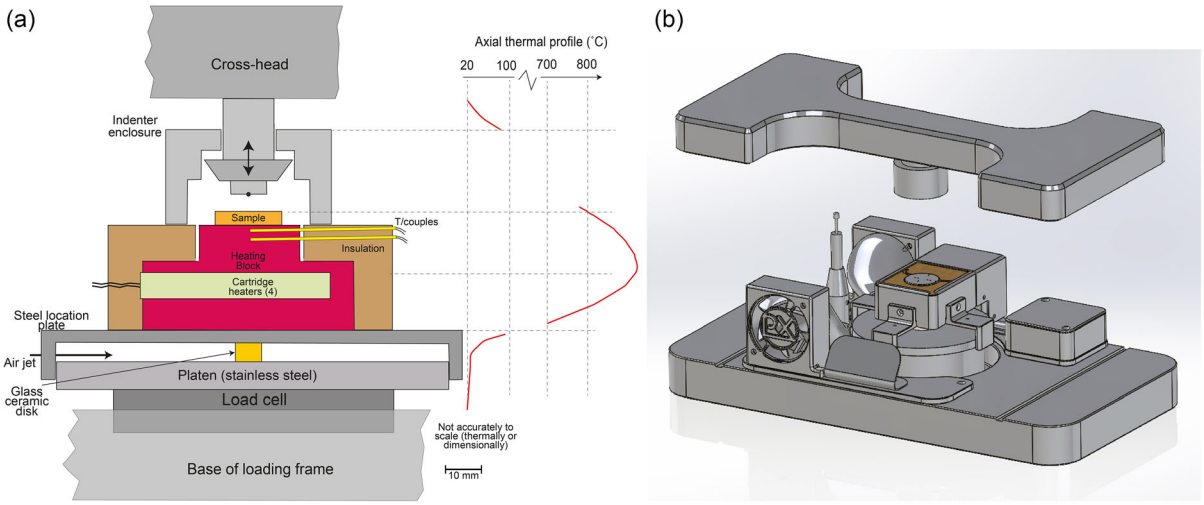

Figure 1. The HT-PIP stage, located within a plastometer: a) a schematic sectional depiction and b) a 3D visualization.

and the sectional area for heat flow through it from the sample is small. The thermal mass of the indenter housing is large compared with the net upward heat flux. The hot zone is thus quite well confined.

The stage has four main components—the heating assembly itself (which locates onto the platen), a plate that bolts onto the baseplate (with cooling fans, linear variable displacement transducer, and connector block attached), the indenter housing assembly (which is bolted to the crosshead), and a box containing the electronic control system. Assembly and disassembly are very quick and easy—it can be carried out in about 10 min. The plastometer is simply plugged into a standard single phase (220/240 V) mains socket. The power requirement is for a theoretical peak of around 2 kW, although the measured peak is about 1.5 kW (during the initial transient when the cartridge heaters are cold and have a low electrical resistance). Steady-state power consumption at the highest operating temperatures is about 0.5 kW.

2.3.2. Thermal Fields and Control of Test Temperature

An important issue with relatively compact systems is that of controlling the thermal field so that the temperature of the sample—or in this case of the part of the sample being tested—can be preselected. For routine testing, it is not always possible to locate a thermocouple within (a drilled hole in) a sample and there are also problems in ensuring that a thermocouple is in good thermal contact with the free surface of the sample. The approach adopted here is to use information about the temperature within the heating block (close to the bottom of the sample) and to infer the sample test temperature from this. A target temperature can thus be set for the governing thermocouple (closest to the top of the heating block), based on the required test temperature and knowledge of the axial thermal profile in and around the sample. This calculation involves both the sample thickness and its thermal conductivity, which are input by the user.

Once a steady state has been reached (and neglecting lateral heat flow—the heater block is well insulated, although there may be some losses from the sample), the thermal profile across the sample will be as shown schematically in **Figure 2**. A heat transfer coefficient (h_i) characterizes the thermal conductance between heating block and sample. This is expected to have a relatively high value (low thermal resistance) because both surfaces are flat and a (small) load is applied to the indenter during heating. However, experimental measurements were needed to establish whether it could be taken to be infinite (no thermal resistance, with $\Delta T_i = 0$).

Thermal conductivities are required for both block and sample. Fortunately, thermal conductivities of metals are fairly insensitive to microstructure and in general can be specified in a similar way to that in which stiffness is handled during PIP testing—i.e., just identifying the base metal or alloy type should be sufficient to allow a suitable value to be ascribed—see below.

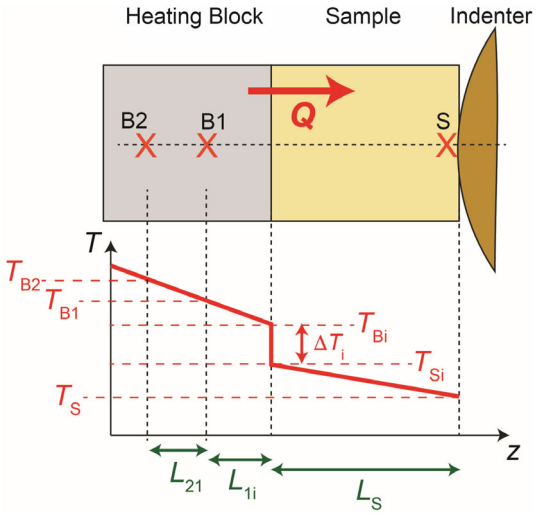

Figure 2. Schematic depiction of the axial thermal profile across the sample and the top part of the heating block, once a steady state has been established. (Thermocouples were located within samples only for trials—this is not done during routine HT-PIP testing).

© 2024 The Author(s). Advanced Engineering Materials published by Wiley-VCH GmbH

15272648, 0, Downloaded from https://onlinelibrary.wiley.com/doi/10.1002/adem.202301073 by National Institute For, Wiley Online Library on [23/09/2024]. See the Terms and Conditions (https://onlinelibrary.wiley.com/terms-and-conditions) on Wiley Online Library for rules of use; OA articles are governed by the applicable Creative Commons License

Moreover, while the presence of impurities and relatively low solute levels can influence (reduce) the conductivity of highly conducting metals such as copper, silver, and aluminum, the exact value is of little significance if it is high—the thermal gradients in the sample will in these cases be low.

Nevertheless, it is important to ascribe reasonably accurate values, particularly for (common) low conductivity metals such as Fe- and Ni-based alloys. Furthermore, these often exhibit a significant dependence on temperature. A representative set of values (with temperature dependence) is tabulated in **Table 2**, with an indication of their source. These data are plotted against temperature in **Figure 3**. Two broad groups can be identified. Values for the main transition metals used for engineering purposes (Fe, Ni, and Ti) fall in the range of 10–50 W m^{-1} K^{-1} (often with some dependence on temperature), whereas alloys based on other common metals (Al, Cu, Ag, etc.), most of which have the highest symmetry (fcc) crystal structure, tend to exhibit higher values (≈100–400 W m^{-1} K^{-1}), with the temperature having relatively little effect. (Ranges are therefore shown in Table 2, but they are plotted as single values in Figure 3: the important point here is simply that as these materials are highly conductive, the exact value is of little significance in the present context.) In terms of practical methodology, expressions in the table can be implemented via a pull-down menu, with the user just choosing the broad alloy type (as is currently done during implementation of PIP for stiffness values).

Table 2. Thermal conductivity data from the literature, including any significant dependence on temperature (T in °C).

Metal	Conductivity, K [W m^{-1} K^{-1}]	Source
Austenitic stainless steel (310)	$12 + 0.015\,T$	[51]
Ferritic stainless steel (HT9)	25	[52]
Medium C steel (0.5%)	$55 - 0.031\,T$	[53]
High C steel (1%)	$40 - 0.012\,T$	[53]
Ni superalloy (Inconel 625)	$11 + 0.016\,T$	[54]
Cast Iron	40	[55]
Titanium (alloy)	21	[56]
Aluminum (alloy)	≈100–200	[57]
Copper (alloy)	≈200–400	[58]

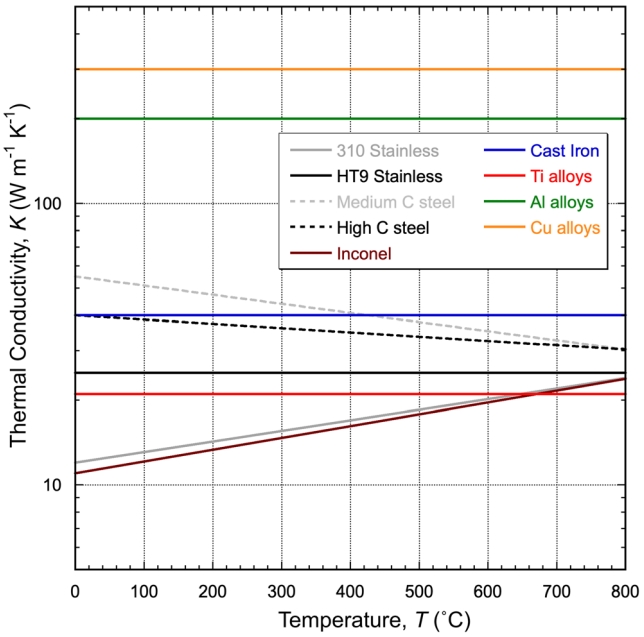

Figure 3. Plot of the thermal conductivity data presented in Table 2. The lines for the Al and Cu alloys are simply for guidance—in the high conductivity regime, the exact value is of little importance for current purposes.

2.3.3. Indentation Procedure

Once the sample is on the heating block, a test temperature is selected. The low thermal inertia of the system ensures that heating (and cooling) rates are quite rapid, with a typical time to reach the maximum test temperature being of the order of 10 min—some details are given below. The indentation itself is normally carried out with a constant penetration velocity of 10 μm s^{-1}, so it typically takes about 20 s (although a few tests were carried out with slower and faster rates of penetration, to check for any time dependence—i.e., creep effects). A small load (≈35 N) is applied to the system throughout the heating period. This is designed to bring the sample and indenter into close thermal contact, ensuring that the temperature in this vicinity is relatively uniform (at the target level). After completion of the indentation, the furnace is switched off (but the fans remain on). The time needed for the sample to cool sufficiently for the profilometry to be carried out—i.e., to reach about 50 °C—depends on the test temperature, but is less than 30 min. Typically, each test was repeated 2 or 3 times. In general, the reproducibility of measured indent profiles was high.

2.3.4. Profilometry and Convergence on Optimized Stress–Strain Relationship

As noted in the Introduction, the FEM model used to simulate the indentation procedure and its iterative use to converge on the optimal solution are fully described in previous publications.[12,13,19,20] This solution takes the form of a best-fit set of Voce parameter values, so that an optimized true stress–true plastic strain relationship is obtained. This can be used for various purposes, including the simple one of converting it (via analytical equations) to the nominal stress–nominal strain relationship that is the immediate outcome of a tensile test (up to the peak, which usually corresponds to the onset of necking). It can also be used in other FEM models, for example, ones that describe the behavior of components under service conditions.

The standard version of the FEM model itself is 2D (radially symmetric) and is implemented via commercial code supplied by COMSOL. The mesh contains about 5000 volume elements, all second-order quadrilateral and/or triangular. Convergence is achieved via a fitting parameter (S_{red}) that characterizes the misfit between measured and modeled residual indent profiles. This parameter, which is a dimensionless, positive number, has a value of zero for perfect fit, but for optimized agreement it might typically have a value of about 10^{-4}. Details of the convergence procedure followed in parameter space are supplied in previous

© 2024 The Author(s). Advanced Engineering Materials published by Wiley-VCH GmbH

15272648, 0, Downloaded from https://onlinelibrary.wiley.com/doi/10.1002/adem.202301073 by National Institute For, Wiley Online Library on [23/09/2024]. See the Terms and Conditions (https://onlinelibrary.wiley.com/terms-and-conditions) on Wiley Online Library for rules of use; OA articles are governed by the applicable Creative Commons License

publications. This operation is no different for HT-PIP than for standard room temperature operation.

A point to note, however, concerning HT-PIP operation is that the stiffness (Young's modulus), which is an input parameter for the modeling, may differ from the corresponding value at ambient temperature. Some published measurements may be open to question, partly because of the possibility of creep deformation, but there is work[33] based on theoretical (interatomic bond strength) calculations that is expected to be reliable. In general, the dependence on temperature is relatively weak, but significant changes might in some cases be expected over the HT-PIP testing range. For example,[33] the stiffness of Ni falls from around 200 GPa at room temperature to 150 GPa at 800 °C ($T/T_f \approx 0.62$). The outcome of PIP testing does not have a high sensitivity to the stiffness, but a change such as this may need to be taken into account.

Overall, there are naturally certain ways in which the HT-PIP test procedure differs from that at room temperature, although none of them are very fundamental. The logic path for HT-PIP testing is depicted in **Figure 4**. The initial part involves specifying certain properties of the sample (at the test temperature). A small amount of lubricating grease is put on the sample before heating is started. This ensures that the friction coefficient is in a suitable range (relatively small) and also helps in reducing oxide formation. It is removed after cooling to room temperature (before the profilometry is carried out). As described in previous publications, a stylus profilometer is used, with a resolution of around ±1 μm. Scans are obtained in several different directions (all passing through the central axis of indentation), partly to check for the possible presence of anisotropy in the sample. Heating to the test temperature is under software control, as is the indentation, cooling, and profilometry. Inferring of stress–strain curves is thus essentially no different from the procedure at room temperature, although potential effects of creep should be noted–see Section 4.2.

3. HT-PIP Testing Characteristics

3.1. Control over the Thermal Field

An example set of thermal histories is shown in **Figure 5**. For these experiments, in addition to the thermocouples in the heating block, one was located in a hole drilled into the sample from the side (as shown in Figure 2), with its end located on the axis of the system, close to the free surface. The test temperature is typically reached in no more than about 10 min. There is good agreement between measured and modeled histories for the sample surface temperature—details of the model are given below.

Several thermal trials of this type were carried out, with different sample materials, thicknesses, and target temperatures, and steady-state readings of the three thermocouples were recorded. Some results are shown in **Table 3**, with the distances relating to the thermocouple locations indicated in Figure 2. The heat flux values shown were obtained from the two measured temperatures in the heating block, the distance between them and the thermal conductivity of the block material for the temperature range concerned (Table 2), using:

$$Q = \frac{(T_{B2} - T_{B1})}{L_{21}} K_B \tag{1}$$

The interfacial heat transfer coefficient, h_i, can be estimated from the heat flux (provided the temperature drop across the interface ΔT_i is known), using the simple relationship:

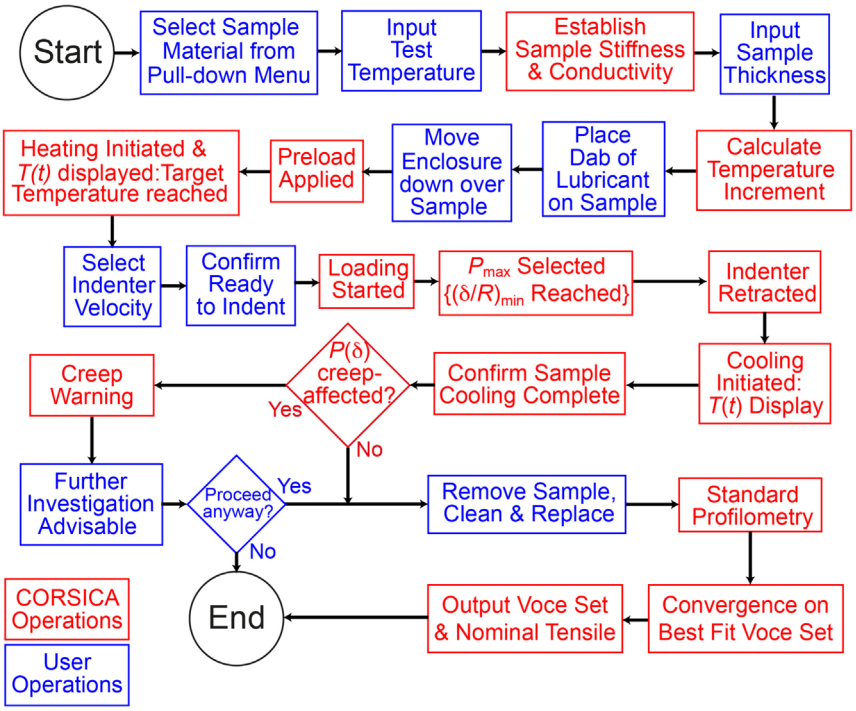

Figure 4. Logic path for HT-PIP testing.

© 2024 The Author(s). Advanced Engineering Materials published by Wiley-VCH GmbH

15272648, 0, Downloaded from https://onlinelibrary.wiley.com/doi/10.1002/adem.202301073 by National Institute For, Wiley Online Library on [23/09/2024]. See the Terms and Conditions (https://onlinelibrary.wiley.com/terms-and-conditions) on Wiley Online Library for rules of use; OA articles are governed by the applicable Creative Commons License

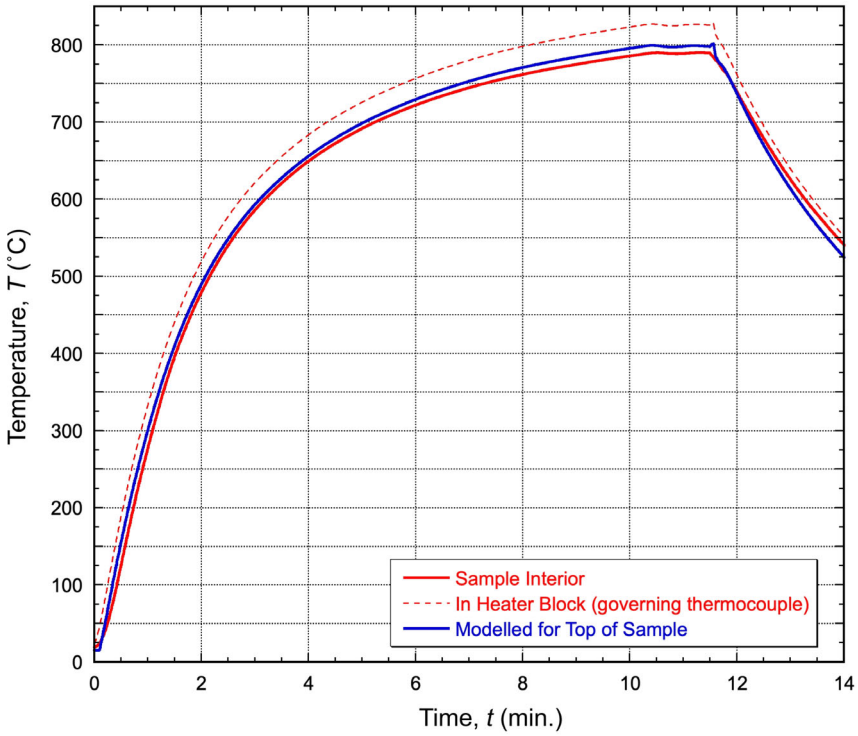

Figure 5. A set of thermal histories, for a 3 mm thick SS310 sample being heated to 800 °C.

Table 3. Steady-state temperatures from a series of heating trials, for the HSS (S690QL) and the Al alloy (2618), all with $L_{21} = L_{1i} = 2$ mm.

Metal	L_S [mm]	Temperatures [°C]			Q [kW m^{-2}]	ΔT_i [°C]	L_S [mm]	Temperatures [°C]			Q [kW m^{-2}]	ΔT_i [°C]
		T_{B2}	T_{B1}	T_S				T_{B2}	T_{B1}	T_S		
HSS	4.25	101	100	96	7	2.2	8.3	106	104	97	14	2.1
HSS	4.25	208	204	195	30	1.6	8.3	217	212	196	38	2.7
HSS	4.25	423	415	391	72	7	8.3	329	322	296	58	5.8
HSS	4.25	533	525	488	78	19	8.3	437	426	389	99	2.6
HSS	4.25	646	634	596	126	10	8.3	561	547	492	136	7.6
HSS	4.25	753	741	696	135	15	8.3	668	651	581	178	7.8
HSS							8.3	803	785	699	202	15
Al alloy	3.4	103	102	98	7	2.7	–	–	–	–	–	–
Al alloy	3.4	212	209	201	22	4	–	–	–	–	–	–
Al alloy	3.4	324	318	305	49	5	–	–	–	–	–	–
Al alloy	3.4	428	420	402	72	7	–	–	–	–	–	–

$$h_i = \frac{Q}{\Delta T_i} \tag{2}$$

This interfacial temperature drop, which is equal to $(T_{Bi} - T_{Si})$, can be estimated via extrapolation to the interface of the thermal gradients in block and sample (recognizing that the heat flux is the same in both, provided that a steady state has been established and that heat flow is predominantly axial). This leads to

$$T_{Bi} = T_{B1} - (T_{B2} - T_{B1})\left(\frac{L_{1i}}{L_{21}}\right) \tag{3}$$

$$T_{Si} = T_S + (T_{B2} - T_{B1})\left(\frac{L_S}{L_{21}}\right)\left(\frac{K_B}{K_S}\right) \tag{4}$$

The heat fluxes in Table 3 are in the range 5–200 kW m^{-2}, rising as the temperature is increased and being higher for thicker samples. The inferred values of ΔT_i are all low, although they rise with increasing temperature (and heat flux).

© 2024 The Author(s). Advanced Engineering Materials published by Wiley-VCH GmbH

15272648, 0, Downloaded from https://onlinelibrary.wiley.com/doi/10.1002/adem.202301073 by National Institute For, Wiley Online Library on [23/09/2024]. See the Terms and Conditions (https://onlinelibrary.wiley.com/terms-and-conditions) on Wiley Online Library for rules of use; OA articles are governed by the applicable Creative Commons License

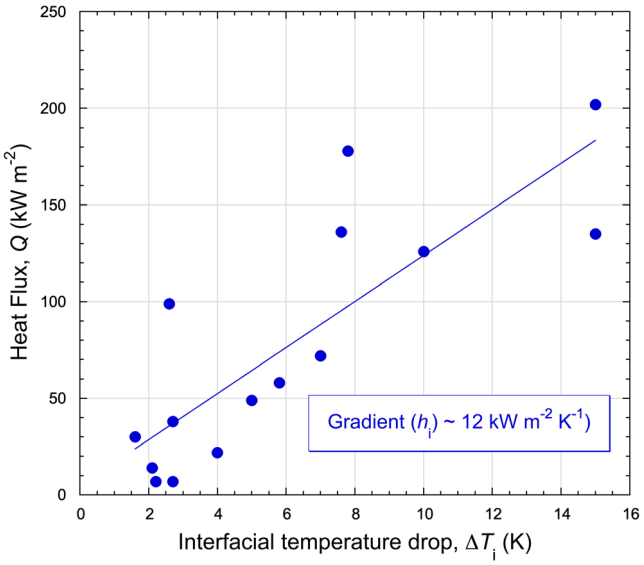

Figure 6. Plot of the data for Q and ΔT_i in Table 3, showing how an estimate is obtained for the interfacial heat transfer coefficient, h_i.

These values can be used to estimate h_i, which is expected to be approximately constant (because it just depends on the physical contact conditions at the interface, which are not expected to vary much). **Figure 6** is a plot of Q against ΔT_i, using the values in Table 3. While there is inevitably some scatter, there is at least an approximately linear trend, with the gradient (h_i) having a (high) value of about 12 kW m^{-2} K^{-1}. It is unsurprising that the interfacial thermal contact is good, leading to relatively small temperature drops, but it is worthwhile to take them into account.

The required temperature "correction increment" can be written as the sum of the three contributions:

$$T_{B1} - T_S = \frac{(T_{B1} - T_{B2})L_{1i}}{L_{21}} + \frac{Q}{h_i} + \frac{(T_{B1} - T_{B2})L_s}{L_{21}}\left(\frac{K_B}{K_s}\right)$$
$$\therefore T_{B1} - T_S = Q\left(\frac{L_{1i}}{K_B} + \frac{1}{h_i} + \frac{L_S}{K_S}\right) \quad (5)$$

The units here are kW m^{-2} for Q, mm for L, W m^{-1} K^{-1} for K, and kW m^{-2} K^{-1} for h_i. (Use of these units for L, Q, and h_i eliminates the need for conversion factors of 10^3, etc.)

The value of Q to use in this equation could be obtained from Equation (1), but that would require real-time monitoring of T_{B2}—complicating the algorithm considerably. Recognizing that the approximate relation between the target temperature and the heat flux is universal (for this particular setup), it can be estimated from data such as those in Table 3. It can be expressed:

$$Q \approx 30\left(\frac{T_S}{250}\right)^{0.9}\left(\frac{L_S}{3}\right)^{0.9} \text{kW m}^{-2} \quad (6)$$

where T_S is in °C and L_S is in mm. This is evidently an empirical (approximate) equation, which is specific to the thermal characteristics of this setup, but this is all that can be done without detailed (FEM) modeling, which is impractical in the present case. **Figure 7** shows plots of the relationship represented by Equation (5) and (6), for selected cases. Agreement between these modeled curves and the experimental data is good. There is also good agreement between corresponding measured and modeled heat fluxes. It is therefore expected that this procedure can be

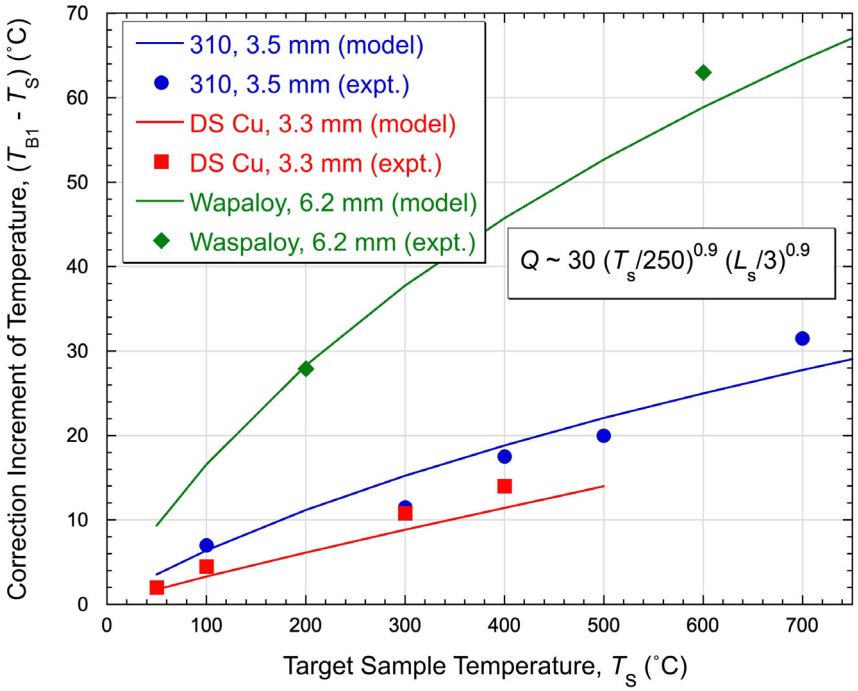

Figure 7. Comparison between modeled (Equation (5) and (6)) and measured values of the incremental temperature correction, as a function of sample temperature.

© 2024 The Author(s). Advanced Engineering Materials published by Wiley-VCH GmbH

15272648, 0, Downloaded from https://onlinelibrary.wiley.com/doi/10.1002/adem.202301073 by National Institute For, Wiley Online Library on [23/09/2024]. See the Terms and Conditions (https://onlinelibrary.wiley.com/terms-and-conditions) on Wiley Online Library for rules of use; OA articles are governed by the applicable Creative Commons License

used to control sample temperatures with an acceptable degree of accuracy.

The picture that emerges from these thermal measurements is that this difference in temperature ($T_{B1} - T_S$) may be relatively small, but is likely to be of the order of several tens of °C and could be as high as 100 °C—becoming larger for higher test temperatures, thicker samples, and materials with lower thermal conductivities. Such differences clearly cannot be neglected, so this "correction" is essential (although it is probably unrealistic to aim for an accuracy of better than about ±10 °C). The procedure is thus that once the target temperature has been selected, the value of Q is obtained from Equation (6) and the necessary governing thermocouple temperature then found from Equation (5), using values of L_S and K_S input by the user—the latter currently being available as an option via a menu of materials. (The values of L_{1i} and K_B, and also h_i, are known and fixed.)

This temperature correction will be of greater significance for metals in the "lower conductivity" category. Not only is the increment raised by the lower conductivity (and hence the higher thermal gradient), but metals in this category are in general more likely to be tested at high temperatures—they tend to have both higher melting temperatures and better microstructural thermal stability. It is also worth noting that the thermal correction, and the error likely to be associated with it, will be lower with thinner samples, particularly for low conductivity metals. The minimum thickness required to ensure that the sample is effectively "semi-infinite" during indentation is around 3 mm (with the 1 mm radius indenter), so a thickness of, say, 3–5 mm may be a good choice in many cases. It may also be helpful to ensure that both the bottom of the sample and the top of the heater block are flat and clean, so that the value of h_i is in the expected range.

3.2. Control of Oxidation and Other Chemical Reactions

A potential concern during HT-PIP testing relates to chemical reactions being stimulated, before and/or during the test. Two types of reaction are possible—sample/indenter and sample/atmosphere. A common sample/indenter reaction involves formation of metal carbides, particularly with diamond indenters. Not all metals are strong carbide-formers, but many of them are. In fact, diamond indenters cannot be used above about 300–400 °C because of erosive oxidation and/or reaction with the sample.[34,35] However, Si_3N_4 indenters are much less likely to react with metallic samples,[36] even at very HT, so this is not a concern for HT-PIP. There are some metals that can form nitrides more stable than Si_3N_4, but even those tend to react only quite slowly, unless the temperature is very high. Silicon nitride can undergo oxidation, but this only becomes significant at temperatures well above the range of interest here.[37,38]

However, sample/atmosphere reaction is always a possibility. Virtually all metals (except gold) have a surface oxide film. Oxidation is always thermodynamically favored (in air) and thickening of an oxide layer can only be avoided by being kinetically very slow. The growth rate of an oxide film normally rises as the temperature is increased (despite the associated decrease in the thermodynamic driving force). The apparently obvious way to inhibit growth is to bring the oxygen partial pressure down to a low level. However, it may need to be very low (ppm range) to reduce the rate of oxidation substantially. This is basically because the rate-determining step is usually the diffusion of ions through the oxide, rather than the rate of adsorption of oxygen at the free surface. There is certainly the possibility of attempting to shroud the sample with an atmosphere having a very low oxygen partial pressure, or possibly with one that would create a reducing environment—for example, one containing hydrogen. In practice, however, there are difficulties, particularly in an enclosure on the HT-PIP heating stage, in which high thermal gradients, and hence strong convection currents, are created. Details are provided in a separate article,[39] which is focused on the issue of oxidation during HT-PIP testing and the potential for employing counter-measures.

While such oxide films (perhaps having a thickness of the order of several tens of microns) are of little significance during tensile testing (of a sample with a diameter of several mm), they could affect HT-PIP testing, in which the response of the near-surface region is of considerable importance. Typical pile-up heights are of the order of a few tens of microns, or sometimes even less, so having a surface layer (with completely different mechanical properties) with a thickness of more than a few microns is a potential concern. However, the low thermal inertia of the HT-PIP setup is advantageous because it allows the time at HT to be limited to just a few minutes. Furthermore, the lubricant that is placed on the sample before heating (and cleaned off before the profilometry) helps to reduce the rate of oxidation. At least in most cases, these measures allow the thickness of any oxide layers to be kept relatively low. (If the effect of a heat treatment is being investigated, then it is recommended that this should be carried out separately and the surface then reground before being tested using HT-PIP.)

4. HT Mechanical Properties

4.1. Indent Profiles

Five materials were tested, both in tension and via HT-PIP, over a range of temperature. All of the materials tested were confirmed (via PIP testing) to be isotropic and homogeneous—the indents were radially symmetric and the same outcomes were obtained from different locations in the as-received materials. In most cases, Voce sets were found that gave excellent agreement between measured and modeled indent profiles, although there were some limitations to this at high temperatures—see below. Examples are shown in **Figure 8**, which are for the SS310 alloy. The procedures for obtaining the model results are fully described in previous publications.[12,13,19,20]

4.2. Stress–Strain Curves

4.2.1. Stainless Steel

Nominal stress–strain curves for SS310 are shown in **Figure 9**. There is good agreement between tensile and PIP, with all cases up to 700 °C being within ±10%. This would be acceptable at room temperature, and there are clearly more potential sources

© 2024 The Author(s). Advanced Engineering Materials published by Wiley-VCH GmbH

15272648, 0, Downloaded from https://onlinelibrary.wiley.com/doi/10.1002/adem.202301073 by National Institute For, Wiley Online Library on [23/09/2024]. See the Terms and Conditions (https://onlinelibrary.wiley.com/terms-and-conditions) on Wiley Online Library for rules of use; OA articles are governed by the applicable Creative Commons License

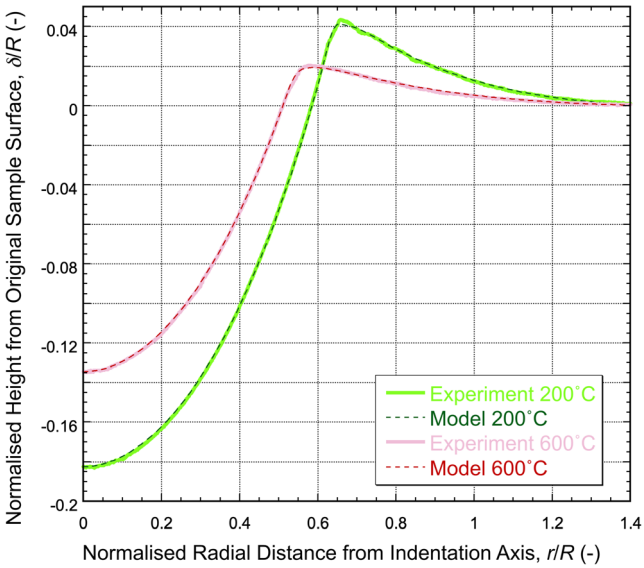

Figure 8. Comparisons between modeled and measured PIP indent profiles, for the SS310, after testing at two different temperatures. (The applied loads were 2.53 kN at 200 °C and 1.518 kN at 600 °C.).

of discrepancy with HT testing, so this level of agreement is encouraging. Following the standard PIP procedure, nominal stress–strain curves are shown only up to the onset of necking (expected to occur at the peak in the plot). These are derived from the true curve, using the standard analytical equations. The tensile plots, on the other hand, are shown up to the point of rupture, so that the "ductility" (nominal strain at failure) can be seen. In fact, this value is not of any intrinsic significance (because it depends on the dimensions of the test-piece), but these portions of the tensile curves are shown for completeness. It is, however, notable that there is significant disagreement between PIP and tensile for the 800 °C case. This is thought to be associated with creep deformation starting to have a significant effect. This is investigated in detail below.

The serrations in the tensile curve for 600 °C were observed in repeat runs and appear to be real. The most likely explanation for them is that they arise from "Suzuki locking," caused by segregation of substitutional solute—presumably Cr and/or Ni in this case—to stacking faults between dissociated pairs of partial dislocations. This is a weaker effect than the more familiar pinning by interstitials (such as carbon), which occurs in a much lower temperature range (because they have much higher mobility, as well as binding more strongly to dislocations). Nevertheless, Suzuki serrations can be noticeable and similar types of curve to the one observed here, occurring in similar temperature ranges, have been reported a number of times for fcc systems,[40–44] together with evidence that the pinning does indeed result from substitutional solute segregating to stacking faults between dissociated partials. Such serrations cannot, however, be reliably detected in load–displacement data acquired during indentation (or in residual indent profiles) because the displacement at any given load is affected by the local response of regions that have reached a wide range of different strains. This "integration" removes the sensitivity to effects occurring throughout the sample at a specific strain (as in a tensile test). A similar limitation applies to initial strain bursting ("Lüders bands") and transitional yielding.

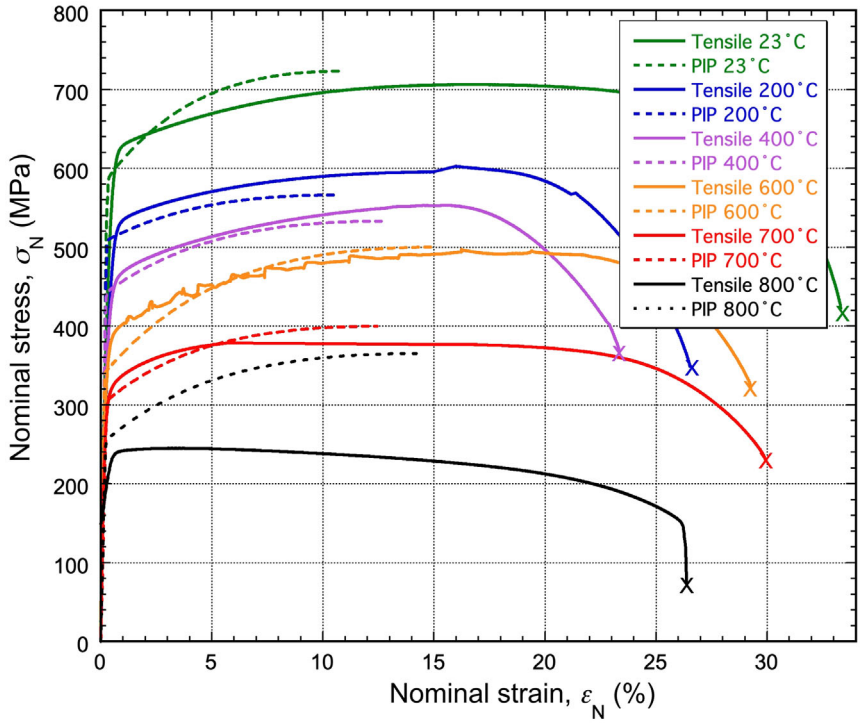

Figure 9. Nominal stress–strain curves for SS310, from HotPIP and tensile testing.

© 2024 The Author(s). Advanced Engineering Materials published by Wiley-VCH GmbH

15272648, 0, Downloaded from https://onlinelibrary.wiley.com/doi/10.1002/adem.202301073 by National Institute For, Wiley Online Library on [23/09/2024]. See the Terms and Conditions (https://onlinelibrary.wiley.com/terms-and-conditions) on Wiley Online Library for rules of use; OA articles are governed by the applicable Creative Commons License

15272648, 0, Downloaded from https://onlinelibrary.wiley.com/doi/10.1002/adem.202301073 by National Institute For, Wiley Online Library on [23/09/2024]. See the Terms and Conditions (https://onlinelibrary.wiley.com/terms-and-conditions) on Wiley Online Library for rules of use; OA articles are governed by the applicable Creative Commons License

4.2.2. High-Speed Steel

Corresponding results for S690QL are shown in **Figure 10**. There is some minor strain bursting at ambient, which disappears at higher temperature. Again, such effects cannot be captured via PIP testing, but its overall significance is minimal. For this material, there is considerable softening between 400 and 600 °C. This change involves going well above the tempering temperature and is associated with coarsening of fine carbides and reconstruction of fine bainitic and twinning structures. These trends—i.e., being harder than the SS310 at room temperature, but ending up softer at around 600 °C—are thus consistent with their microstructural characteristics.

It is, however, clear from Figure 10 that, while the agreement is in general quite good up to 400 °C, substantial discrepancies arise at higher temperatures, with the strain to the apparent onset of necking (peak in the nominal plot) being much lower for the tensile test, followed by a progressive drop in the stress level. This has been investigated in detail for the highest temperature (700 °C). The tensile testing was carried out at three different strain rates (differing by a factor of about 30 between highest and lowest rates). It should be noted, however, that none of these rates (lying in the approximate range of 10^{-2} to 10^{-3} s^{-1}) are outside of what is conventionally regarded as the quasistatic regime (in which no dependence of plastic deformation characteristics on strain rate is normally expected). The sharp differences between the three tensile curves (with the apparent yield stress dropping by a factor of about 50%) clearly indicate that creep effects are highly significant (despite the duration of the test covering only periods of up to about 5–10 min). It should be noted in this context that it is primary creep that is likely to be dominant here and this is often much faster than secondary (steady state) creep, particularly at stress levels close to the yield stress. Creep during a tensile test can certainly lead to a reduction in (nominal) stress with increasing strain, apparent well before necking has become established—this would often be referred to as stress relaxation (under strain control conditions). In fact, for these tensile tests, the stress fell to low levels before final necking and rupture occurred. It may be concluded that creep is having a strong effect on the tensile outcomes over the complete range of strain rate covered in these tests.

The HT-PIP testing at 700 °C was also carried out at different "strain rates" and the PIP-derived stress–strain curves in Figure 10 are shown for two different penetration velocities—the standard one of 10 μm s^{-1} and a fast one of 50 μm s^{-1}. The difference between the two confirms that time-dependent effects can also arise during these tests. In fact, a slow test was also carried out, at 1 μm s^{-1}, but it was not possible to obtain a good fit to the resultant profile using a Voce plasticity curve. The indent profiles for the three cases are shown in **Figure 11**, where it can be seen that the slow profile was certainly being strongly affected by creep—note the much lower load needed to reach the target penetration range (less than half that for the fast case). It is unsurprising that the profile from what was probably creep-dominated indentation could not be well captured using a plasticity relationship. (It may also be noted that the average strain rate during these HT-PIP tests, weighted by the amount of plastic strain being induced at different strain rates,

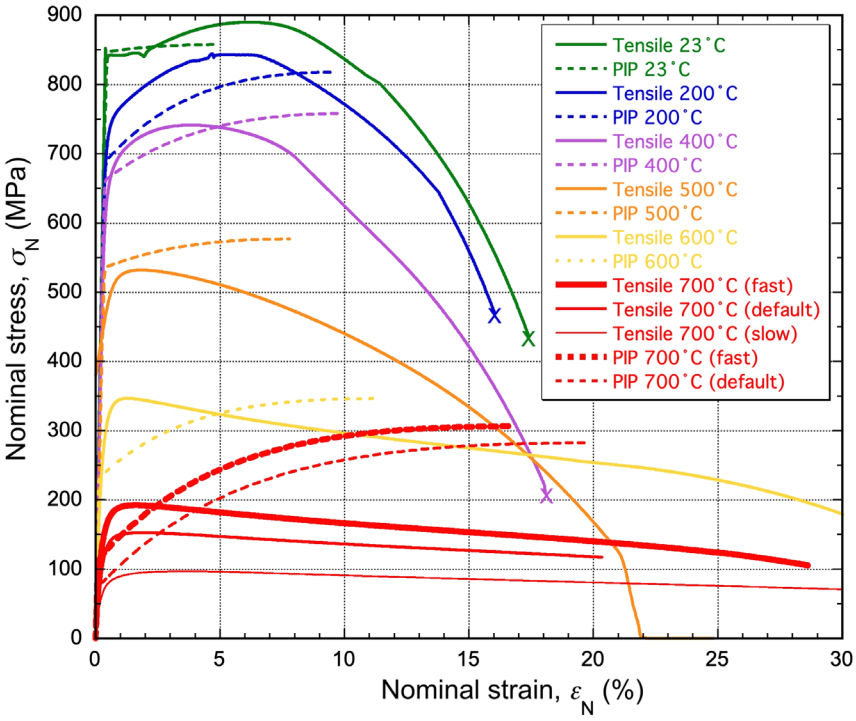

Figure 10. Nominal stress–strain curves for S690QL, from HT-PIP and tensile testing. At 700 °C, tensile tests were carried out with "slow" (7×10^{-4} s^{-1}) and "fast" (2×10^{-2} s^{-1}) strain rates, in addition to the default rate (7×10^{-3} s^{-1}), while the standard PIP testing, with a penetration velocity of 10 μm s^{-1}, was supplemented by a fast one at 50 μm s^{-1}.

 © 2024 The Author(s). Advanced Engineering Materials published by Wiley-VCH GmbH

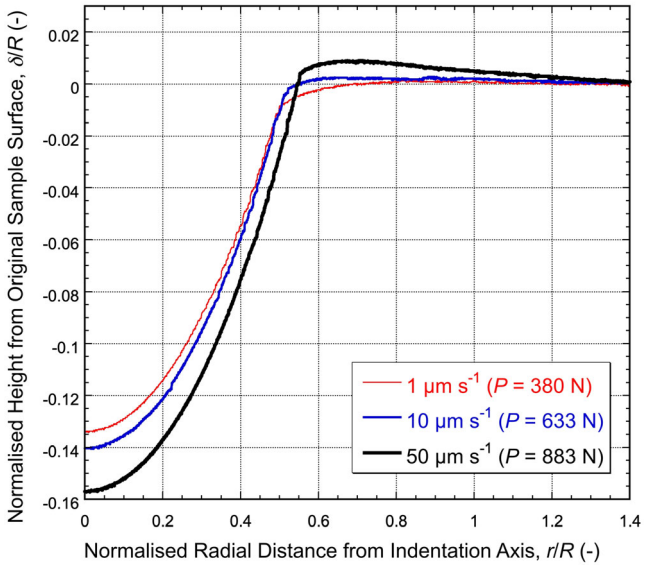

Figure 11. Measured indent profiles after HT-PIP testing of S690QL at 700 °C, carried out with "slow," "standard," and "fast" indenter penetration velocities. The loads needed to penetrate to the depths shown are indicated.

Figure 12. Photograph of two samples, which were obtained by interrupting tensile tests after a strain of 10%, with the tests being carried out at temperatures of 200 and 700 °C.

was calculated via FEM simulation to be $\approx 2.5 \times 10^{-2}$, 5×10^{-3}, and $5 \times 10^{-4}\ s^{-1}$, respectively, for these fast, standard, and slow cases: these values cover a similar range to those in the tensile tests).

As a further confirmation that the creep-affected tensile stress–strain curves are quite different from those representing pure plasticity, two interrupted tests were carried out, up to a strain of 10%. This was done, using the standard strain rate of $7 \times 10^{-3}\ s^{-1}$, at temperatures of 200 and 700 °C. It can be seen from Figure 10 that, in both cases, this strain is well past the peak in the plot. Conventional interpretation of such curves would therefore envisage that a sample strained to this level should contain a well-defined neck, with virtually all of the recorded straining in this regime being due to its development. **Figure 12** is a photograph of the two samples obtained in this way. While the sample tested at 200 °C does indeed contain a neck, which has developed to approximately the degree that might have been expected at this strain, there is no trace of a neck in the sample tested at 700 °C. It is clear that, for this case, the progressive post-peak fall in the nominal stress is due to a creep relaxation effect, rather than to the development of a neck.

As indicated in the CORSICA logic path of Figure 4, a check is automatically made on whether creep is likely to be having a significant effect on the outcome (of PIP testing, although, for cases in which the effect during PIP is noticeable, it is also likely that tensile stress–strain curves will be creep-affected). This check is made by monitoring the shape of the load–displacement plot (during penetration at the standard rate of 10 μm s^{-1}). Under purely plastic conditions, this plot is expected to have a positive curvature—so that, if it is fitted to a power law relationship, the value of the exponent is greater than unity. A contribution from creep, however, progressively introduces extra displacement (that will be greater for slower penetration rates). If this contribution is substantial, then the curvature is likely to become negative, corresponding to a fitted power law exponent having a value below unity. A linear relationship, with an exponent value of unity (constant gradient), can be taken to be broadly indicative of the transition regime.

A warning is issued if such a condition is being met (as indicated in the flow chart of Figure 4). Examples are shown in **Figure 13** of load–displacement curves for cases (temperatures) in which the effects of creep are negligible or strong. (These two cases are the ones for which photos are shown in Figure 12). **Figure 14** is a summary plot of n values obtained in this way for the Al-2618 alloy, over a range of temperature—details of the stress–strain curves obtained for this alloy are given in

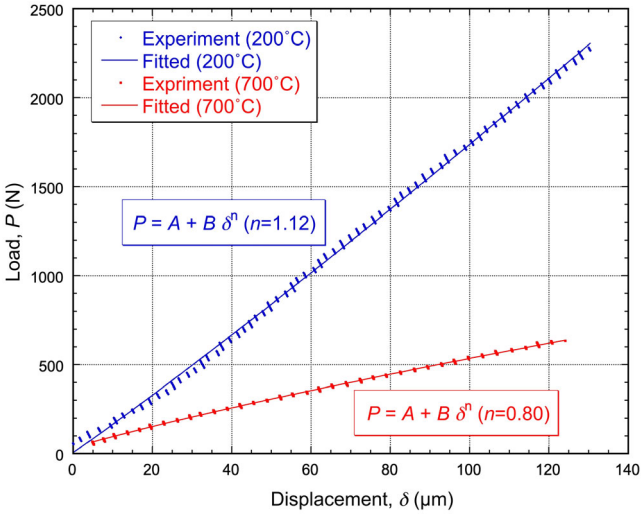

Figure 13. Measured load–displacement plots obtained during indenter penetration at the standard velocity of 10 μm s^{-1}, for PIP testing of S690QL samples at temperatures of 200 and 700 °C. Also shown are power law curves, with best-fit exponent values.

© 2024 The Author(s). Advanced Engineering Materials published by Wiley-VCH GmbH

15272648, 0, Downloaded from https://onlinelibrary.wiley.com/doi/10.1002/adem.202301073 by National Institute For, Wiley Online Library on [23/09/2024]. See the Terms and Conditions (https://onlinelibrary.wiley.com/terms-and-conditions) on Wiley Online Library for rules of use; OA articles are governed by the applicable Creative Commons License

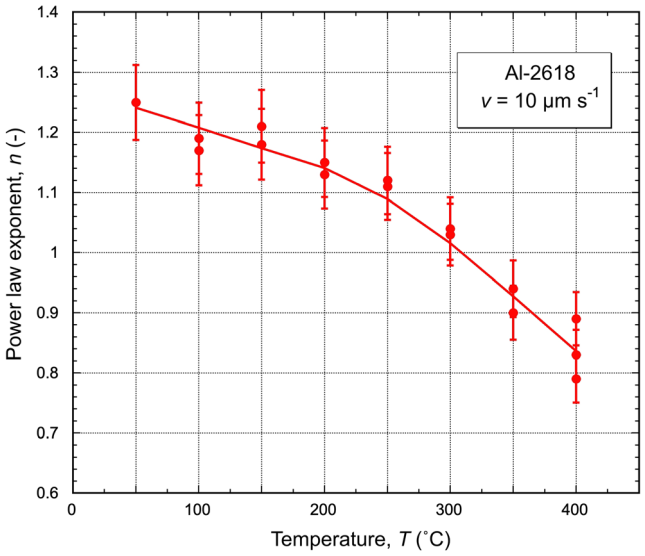

Figure 14. Plot of measured values of the power law exponent against test temperature, derived from load–displacement data obtained during PIP testing of Al-2618, with a penetration velocity of 10 μm s^{-1}.

Section 4.2.4. There is clearly scope for using this value (acquired in real time during standard indentation) to decide whether a "creep warning" message is needed.

For standard PIP testing, the inferred stress–strain curves are constrained to be Voce plots (converted to nominal form), so there is no scope for replicating the stress relaxation effects created by creep in the tensile tests. It could be argued that the PIP outcome for a given average strain rate could be regarded as a plasticity relationship that takes account of creep, in a similar way to a tensile curve being tagged with an associated strain rate. However, in practice this is similarly unsatisfactory, quite apart from the possibility that it may not be possible to obtain a Voce curve giving good fit to the measured profile. Outcomes will, in practice, depend on the sensitivity of the creep rate to the stress (commonly in the form of an exponent)—particularly for PIP testing, in which there is a wide range of local stress levels.

However, there may be potential for using PIP outcomes obtained with a range of penetration velocities to infer both plasticity and creep characteristics, using an extension of the inverse FEM approach applied to plasticity in the standard procedure. Something similar could also be done for tensile test outcomes. There will certainly be many cases for which creep effects are small or negligible, but these outcomes for S690QL at 700 °C (and even at 500 °C) illustrate clearly that there is potential for associated changes to be dramatic, such that making comparisons between tensile and PIP-derived curves must be approached with considerable care. Monitoring of the load–displacement plot during PIP is a good way of checking on creep contributions, although repeating tensile tests with different strain rates may also be advisable. (This should be standard procedure for HT tensile testing, irrespective of whether PIP testing is being done.) Ideally, both the pure plasticity and the pure creep characteristics of a metal (at a particular temperature) should be captured, although the nature of the equations used is different in the two cases (and primary creep will need to be included in the formulation). Once this information has been obtained, it should be possible to model any given loading scenario (in which both occur simultaneously).

4.2.3. Ni-Based Superalloy

Corresponding results for the Waspaloy are shown in **Figure 15**. This is a material that tends to retain its strength up to relatively HT and the changes in the stress–strain curve over the range studied are not so great. In fact, there is very little change between 300 and 700 °C, with good agreement between tensile and HT-PIP outcomes. There is apparently no significant contribution from creep over this temperature range. This is broadly consistent with known information[45,46] about its creep characteristics.

4.2.4. Age-Hardening Al Alloy

The Al-2618 alloy can be used to highlight some of the issues related to microstructural stability when testing at HT. For this alloy[47,48] the ageing temperature is about 190–200 °C. This is higher than for most Al-based age-hardening alloys and indeed it is specifically designed to be suitable for HT applications. Nevertheless, mechanical testing at or above this temperature range is likely to involve thermal histories that will cause changes in the properties at the test temperature, via over-ageing prior to the test. The tests themselves were completed in less than a minute, so it is unlikely that much over-ageing took place during this period. However, the prior thermal histories are likely to have an effect, so the same treatment (a heating rate of 20 K min^{-1}, followed by a 20 min soak at the test temperature) was used for both types of test, to ensure that the over-ageing effect was the same in each case. It should also be noted that, when materials become soft in this way, there is in general greater potential for creep to affect tensile tests, as shown in Figure 10.

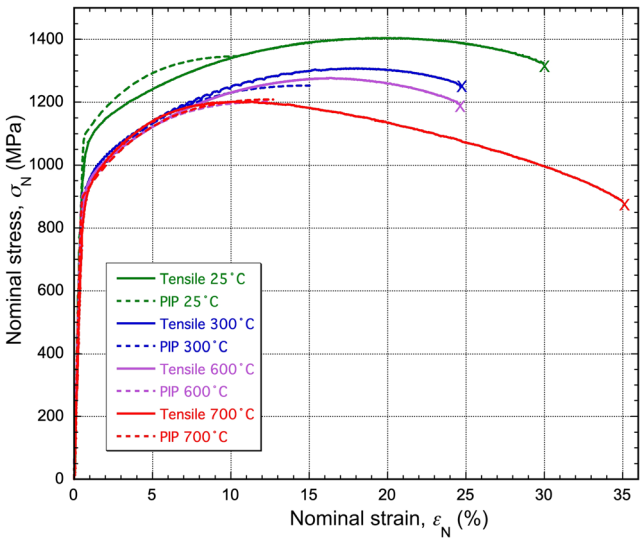

Figure 15. Nominal stress–strain curves for Waspaloy, from HT-PIP and tensile testing.

© 2024 The Author(s). Advanced Engineering Materials published by Wiley-VCH GmbH

15272648, 0, Downloaded from https://onlinelibrary.wiley.com/doi/10.1002/adem.202301073 by National Institute For, Wiley Online Library on [23/09/2024]. See the Terms and Conditions (https://onlinelibrary.wiley.com/terms-and-conditions) on Wiley Online Library for rules of use; OA articles are governed by the applicable Creative Commons License

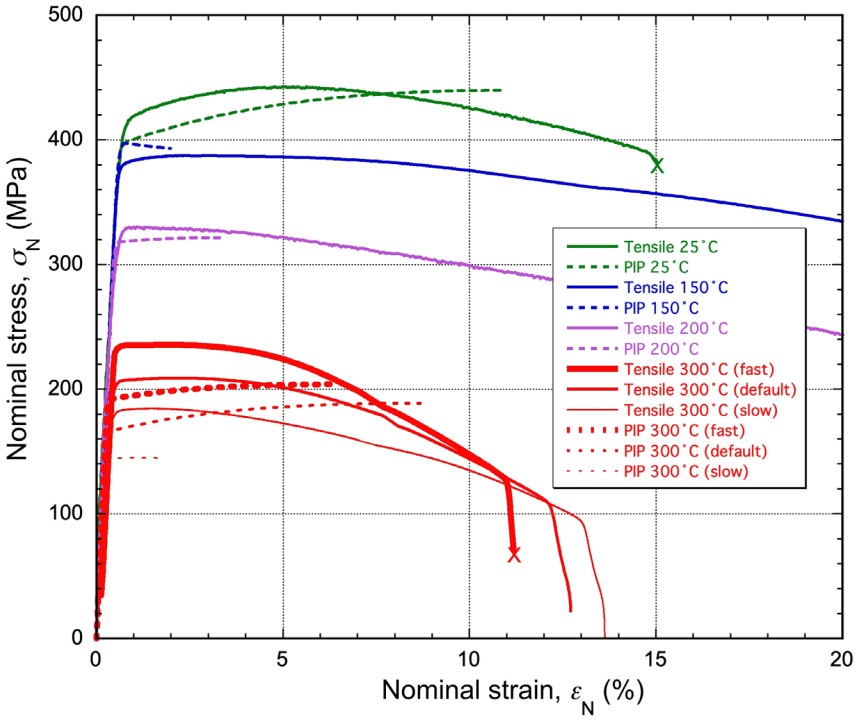

Figure 16. Nominal stress–strain curves for Al-2618, from HT-PIP and tensile testing. At 300 °C, tensile tests were carried out with fast ($2 \times 10^{-2}\,s^{-1}$) and slow ($7 \times 10^{-4}\,s^{-1}$) strain rates, in addition to the default rate ($7 \times 10^{-3}\,s^{-1}$), while the PIP tests were carried out with fast ($50\,\mu m\,s^{-1}$), default ($10\,\mu m\,s^{-1}$), and slow ($1\,\mu m\,s^{-1}$) penetration velocities.

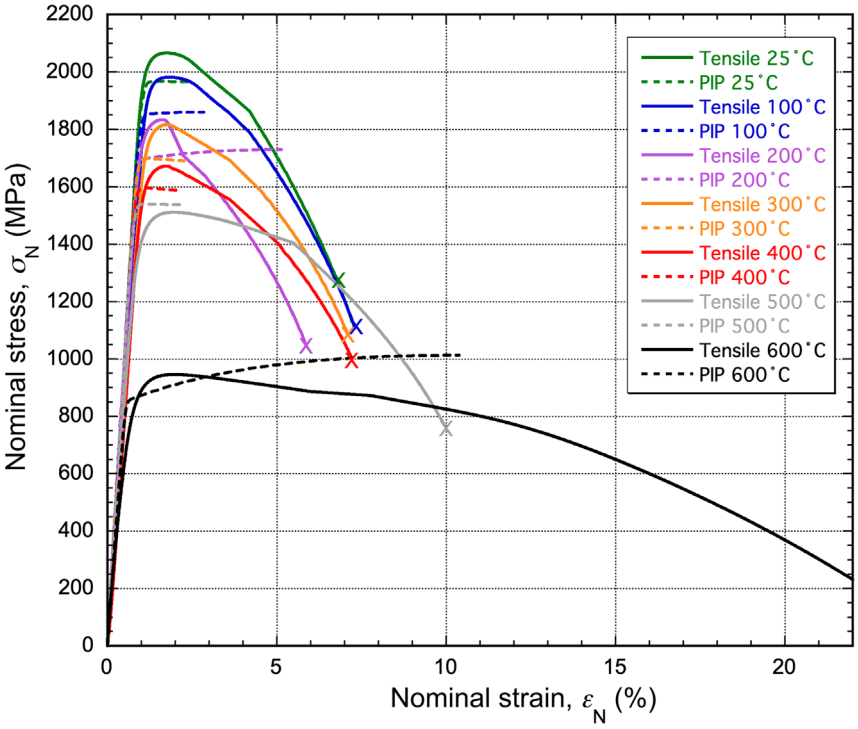

Figure 17. Nominal stress–strain curves for C-300, from HT-PIP and tensile testing.

© 2024 The Author(s). Advanced Engineering Materials published by Wiley-VCH GmbH

15272648, 0, Downloaded from https://onlinelibrary.wiley.com/doi/10.1002/adem.202301073 by National Institute For, Wiley Online Library on [23/09/2024]. See the Terms and Conditions (https://onlinelibrary.wiley.com/terms-and-conditions) on Wiley Online Library for rules of use; OA articles are governed by the applicable Creative Commons License

15272648, 0, Downloaded from https://onlinelibrary.wiley.com/doi/10.1002/adem.202301073 by National Institute For, Wiley Online Library on [23/09/2024]. See the Terms and Conditions (https://onlinelibrary.wiley.com/terms-and-conditions) on Wiley Online Library for rules of use; OA articles are governed by the applicable Creative Commons License

A comparison is shown in **Figure 16** between tensile and PIP-derived curves for the Al alloy. The curves do indicate that, for temperatures of 150 °C and above, there is little or no work hardening. (This is certainly expected in this temperature range for this alloy.) The peaks are therefore expected to occur at low strains, even if there is no creep. The curves for 200 and 300 °C do have peaks at low strains, but it is likely that these tests were affected by creep—particularly at 300 °C. The obvious way to check on this is to carry out the tensile test with a range of strain rates—as has been done for the 300 °C case in Figure 16. A similar effect is observed to that in Figure 10 for 700 °C, although the differences are less dramatic—the apparent fall in "yield stress" between fastest and slowest strain rates being about 25%, compared with 50% for the S690QL alloy at 700 °C. This again leaves the problem that there is in fact no well-defined yield stress (and also no meaningful UTS)—or at least there is no way of accessing these values via stress–strain curves that have been affected by creep in this way. It can also be seen in Figure 16 that different PIP curves were obtained with different penetration velocities, but again the shapes of PIP and tensile curves are different (and neither represent the pure plastic characteristics). The PIP outcomes may still give some indication of the tensile "plateau" levels—at least for cases in which creep is not completely dominating the outcome, but it is important to recognize that neither PIP nor tensile plots for this temperature are "genuine" stress–strain curves.

4.2.5. Maraging Steel

Finally, certain points can be noted for the C-300, which has an ageing temperature[49] of around 400–500 °C. Its HT strength is largely due to the presence of fine Ni_3Ti needle-like precipitates that are strongly resistant to coarsening in this temperature range.[50] Above 500 °C, the strength does drop sharply as over-ageing becomes rapid. The same prior thermal histories were again used for the two types of test. The curves are shown in **Figure 17**. Up to 500 °C there is good agreement between PIP and tensile curves, with very little work hardening and a yield stress that does not fall much over this temperature range. At 600 °C, however, the tensile curve is starting to become "creep-affected," with the onset of necking no longer coinciding with the peak in the curve. In this particular case, the yield stress obtained via PIP testing is close to the stress level at the peak in the tensile curve, but the subsequent shape is not captured. The deviations will certainly be greater at higher temperatures.

5. Conclusions

The following conclusions may be noted: 1) The viability of carrying out HT-PIP testing (to obtain stress–strain relationships) at elevated temperatures (up to 800 °C) has been demonstrated and a commercial setup is described. 2) The thermal characteristics of the setup have been investigated. It has a relatively low thermal inertia, such that the heating period is typically no more than about 10 min and the time spent close to the test temperature is just a couple of minutes or so. 3) The temperature at the top of the sample, where indentation is carried out, is related to that of the governing thermocouple, located within the heating block. Heat flow analysis has been used to establish this relationship, which depends on the thickness and conductivity of the sample, as well as the target temperature. This temperature difference (between that of the governing thermocouple and that at the top of the sample) is typically a few tens of °C, but it could be as high as 100 °C in some cases. 4) In general, good levels of agreement are observed between stress–strain curves obtained via HT-PIP and from conventional tensile testing. However, particularly at very high temperatures, the stress–strain curves obtained via both tensile and HT-PIP testing may be significantly affected by creep (despite the test durations being short in both cases). This can be investigated experimentally by carrying out the tests with different strain rates (by changing the tensile displacement rate or the HT-PIP indenter penetration velocity). Significant differences in the outcomes for different strain rates indicate that these curves are "creep-affected." Furthermore, automated monitoring of the shape of the load–displacement plot can be used to detect whether this is the case. In such cases, use of the standard PIP procedure to capture the progressive creep-driven stress relaxation that is likely to occur during a tensile test is not possible.

Acknowledgements

Financial support for T.W.C. is acknowledged from EPSRC, via (grant no. EP/I038691/1). Relevant support has also been received from the Leverhulme Trust, in the form of an International Network grant (IN-2016-004) and an Emeritus Fellowship (EM/2019-038/4). In addition, an ongoing Innovate UK grant (project no. 10006185) covers work in this area and JEC is in receipt of a Future Leaders grant from Innovate UK (MR/W01338X/1), which is focused on development of the PIP technique.

Conflict of Interest

The authors declare no conflict of interest.

Data Availability Statement

The data that support the findings of this study are available from the corresponding author upon reasonable request.

Keywords

creep, high temperatures, indentation plastometry, stress–strain curves, tensile testing

Received: July 14, 2023
Revised: July 29, 2024
Published online:

[1] B. X. Xu, X. Chen, *J. Mater. Res.* **2010**, *25*, 2297.
[2] A. H. Mahmoudi, S. H. Nourbakhsh, R. Amali, *J. Test. Eval.* **2012**, *40*, 211.
[3] R. O. Oviasuyi, R. J. Klassen, *J. Nucl. Mater.* **2013**, *432*, 28.
[4] C. Yu, Y. H. Feng, R. Yang, G. J. Peng, Z. K. Lu, T. H. Zhang, *J. Mater. Res.* **2014**, *29*, 1095.
[5] S. Pathak, S. R. Kalidindi, *Mater. Sci. Eng. R* **2015**, *91*, 1.

 © 2024 The Author(s). Advanced Engineering Materials published by Wiley-VCH GmbH

[6] J. S. Weaver, S. R. Kalidindi, *Mater. Des.* **2016**, *111*, 463.
[7] K. Jeong, H. Lee, O. M. Kwon, J. Jung, D. Kwon, H. N. Han, *Mater. Des.* **2020**, *196*, 109104.
[8] J. E. Campbell, H. Zhang, M. Burley, M. Gee, A. T. Fry, J. Dean, T. W. Clyne, *Adv. Eng. Mater.* **2021**, *23*, 2001496.
[9] C. Heinrich, A. M. Waas, A. S. Wineman, *Int. J. Solids Struct.* **2009**, *46*, 364.
[10] J. Dean, J. M. Wheeler, T. W. Clyne, *Acta Mater.* **2010**, *58*, 3613.
[11] D. K. Patel, S. R. Kalidindi, *Acta Mater.* **2016**, *112*, 295.
[12] J. Dean, T. W. Clyne, *Mech. Mater.* **2017**, *105*, 112.
[13] J. E. Campbell, R. P. Thompson, J. Dean, T. W. Clyne, *Mech. Mater.* **2018**, *124*, 118.
[14] L. Meng, P. Breitkopf, B. Raghavan, G. Mauvoisin, O. Bartier, X. Hernot, *Int. J. Mater. Form.* **2019**, *12*, 587.
[15] H. Xue, J. X. He, W. N. Jia, J. L. Zhang, S. Wang, S. Zhang, H. L. Yang, Z. Wang, *Structures* **2020**, *28*, 2752.
[16] J. Lee, C. Lee, B. Kim, *Mater. Des.* **2009**, *30*, 3395.
[17] W. Z. Yao, C. E. Krill, B. Albinski, H. C. Schneider, J. H. You, *J. Mater. Sci.* **2014**, *49*, 3705.
[18] M. Z. Wang, J. J. Wu, Y. Hui, Z. K. Zhang, X. P. Zhan, R. C. Guo, *Mater. Sci. Eng. A* **2017**, *679*, 143.
[19] J. E. Campbell, R. P. Thompson, J. Dean, T. W. Clyne, *Acta Mater.* **2019**, *168*, 87.
[20] T. W. Clyne, J. E. Campbell, *Testing of the Plastic Deformation of Metals*, Cambridge University Press, Cambridge, U.K. **2021**.
[21] W. Gu, J. E. Campbell, Y. T. Tang, H. Safaie, R. Johnston, Y. Gu, C. Pleydell-Pearce, M. Burley, J. Dean, T. W. Clyne, *Adv. Eng. Mater.* **2022**, *24*, 2101645.
[22] M. Warwick, H. Vaka, C. Z. Fang, J. Campbell, J. Dean, T. W. Clyne, *Steel Res. Int.* **2023**, *94*, 2200920.
[23] Y. T. Tang, J. E. Campbell, M. Burley, J. Dean, R. C. Reed, T. W. Clyne, *Materialia* **2021**, *15*, 101017.
[24] T. J. F. Southern, J. E. Campbell, K. I. Kourousis, B. Mooney, Y. T. Tang, T. W. Clyne, *Steel Res. Int.* **2023**, *94*, 2200881.
[25] R. Reiff-Musgrove, M. Gaiser-Porter, W. Gu, J. E. Campbell, P. Lewis, A. Frehn, A. D. Tarrant, Y. T. Tang, M. Burley, T. W. Clyne, *Adv. Eng. Mater.* **2023**, *25*, 2201479.
[26] M. Burley, J. E. Campbell, R. Reiff-Musgrove, J. Dean, T. W. Clyne, *Adv. Eng. Mater.* **2021**, *23*, 2001478.
[27] S. Ooi, R. Reiff-Musgrove, M. Gaiser-Porter, M. Steinbacher, I. Griffin, J. E. Campbell, M. Burley, C. M. Warwick, H. Vaka, T. W. Clyne, *Adv. Eng. Mater.* **2022**, *25*, 2201512.
[28] J. E. Campbell, M. Gaiser-Porter, W. Gu, S. Ooi, M. Burley, J. Dean, T. W. Clyne, *Adv. Eng. Mater.* **2022**, *24*, 2101398.
[29] R. Reiff-Musgrove, W. Gu, J. E. Campbell, J. Reidy, A. Bose, A. Chitrapur, Y. T. Tang, M. Burley, T. W. Clyne, *Adv. Eng. Mater.* **2022**, *24*, 2200642.
[30] T. W. Clyne, J. E. Campbell, M. Burley, J. Dean, *Adv. Eng. Mater.* **2021**, *23*, 21004037.
[31] E. Voce, *J. Inst. Met.* **1948**, *74*, 537.
[32] S. Verma, P. Sarkar, P. Pant, *J. Mater. Res.* **2021**, *36*, 3436.
[33] R. Rahemi, D. Y. Li, *Scr. Mater.* **2015**, *99*, 41.
[34] J. M. Wheeler, D. E. J. Armstrong, W. Heinz, R. Schwaiger, *Curr. Opin. Solid State Mater. Sci.* **2015**, *19*, 354.
[35] J. M. Wheeler, R. A. Oliver, T. W. Clyne, *Diamond Related Mater.* **2010**, *19*, 1348.
[36] E. H. Andrews, *J. Mater. Sci.* **1966**, *1*, 377.
[37] M. Maeda, K. Nakamura, M. Yamada, *J. Mater. Sci.* **1990**, *25*, 3790.
[38] T. Narushima, T. Goto, T. Hirai, Y. Iguchi, *Mater. Trans. JIM* **1997**, *38*, 821.
[39] P. J. McKeown, M. Gaiser-Porter, J. R. Miller, Y. T. Tang, J. E. Campbell, T. W. Clyne, *Mater. Sci. Eng. A* **2024**, in preparation.
[40] H. Saka, *Philos. Mag. A* **1983**, *47*, 131.
[41] T. Kamino, Y. Ueki, H. Hamajima, K. Sasaki, K. Kuroda, H. Saka, *Philos. Mag. Lett.* **1992**, *66*, 27.
[42] Y. Kaneko, K. Kaneko, A. Nohara, H. Saka, *Philos. Mag. A* **1995**, *71*, 399.
[43] A. Chiba, M. S. Kim, *Mater. Trans.* **2001**, *42*, 2112.
[44] Z. W. Jiang, L. L. Zhu, L. X. Yu, B. A. Sun, Y. Cao, Y. H. Zhao, Y. Zhang, *Mat. Sci. Eng. A* **2021**, *820*, 141575.
[45] B. Wilshire, P. J. Scharning, *Mat. Sci. Tech.* **2009**, *25*, 242.
[46] M. Whittaker, W. Harrison, C. Deen, C. Rae, S. Williams, *Materials* **2017**, *10*, 61.
[47] I. N. A. Oguocha, S. Yannacopoulos, *Mater. Sci. Eng. A* **1997**, *231*, 25.
[48] J. H. Wang, D. Q. Yi, X. P. Su, F. C. Yin, *Mater. Charact.* **2008**, *59*, 965.
[49] W. Sha, *Scr. Mater.* **2000**, *42*, 549.
[50] F. Zhu, Y. F. Yin, R. G. Faulkner, *Mater. Sci. Technol.* **2011**, *27*, 395.
[51] J. Blumm, A. Lindemann, B. Niedrig, R. Campbell, *Int. J. Thermophysics* **2007**, *28*, 674.
[52] L. Leibowitz, R. A. Blomquist, *Int. J. Thermophysics* **1988**, *9*, 873.
[53] M. J. Peet, H. S. Hasan, H. Bhadeshia, *Int. J. Heat Mass Transf.* **2011**, *54*, 2602.
[54] E. Kaschnitz, L. Kaschnitz, S. Heugenhauser, *Int. J. Thermophysics* **2019**, *40*, 27.
[55] D. Holmgren, *Int. J. Cast Met. Res.* **2005**, *18*, 331.
[56] H. A. Abdel-Aal, M. Nouari, M. El Mansori, *Tribol. Int.* **2009**, *42*, 359.
[57] P. Olafsson, R. Sandstrom, A. Karlsson, *J. Mater. Sci.* **1997**, *32*, 4383.
[58] G. A. Dubskii, K. N. Vdovin, A. A. Nefed'ev, L. G. Egorova, *Russian Metall.* **2018**, *2018*, 252.

© 2024 The Author(s). Advanced Engineering Materials published by Wiley-VCH GmbH

15272648, 0, Downloaded from https://onlinelibrary.wiley.com/doi/10.1002/adem.202301073 by National Institute For, Wiley Online Library on [23/09/2024]. See the Terms and Conditions (https://onlinelibrary.wiley.com/terms-and-conditions) on Wiley Online Library for rules of use; OA articles are governed by the applicable Creative Commons License